

# Revisiting Diffusion Autoencoder Training for Image Reconstruction Quality

Pramook Khungurn<sup>1</sup>, Sukit Seripanitkarn<sup>2</sup>, Phonphrm Thawatdamrongkit<sup>2</sup>, Supasorn Suwajanakorn<sup>2</sup>

<sup>1</sup>pixiv, Inc.

<sup>2</sup>VISTEC

pong@pixiv.co.jp

{sukit.s.s23, phonphrm.t.s23, supasorn.s}@vistec.ac.th

## Abstract

*Diffusion autoencoders (DAEs) are typically formulated as a noise prediction model and trained with a linear- $\beta$  noise schedule [22] that spends much of its sampling steps at high noise levels. Because high noise levels are associated with recovering large-scale image structures and low noise levels with recovering details, this configuration can result in low-quality and blurry images. However, it should be possible to improve details while spending fewer steps recovering structures because the latent code should already contain structural information. Based on this insight, we propose a new DAE training method that improves the quality of reconstructed images. We divide training into two phases. In the first phase, the DAE is trained as a vanilla autoencoder by always setting the noise level to the highest, forcing the encoder and decoder to populate the latent code with structural information. In the second phase, we incorporate a noise schedule that spends more time in the low-noise region [23], allowing the DAE to learn how to perfect the details. Our method results in images that have accurate high-level structures and low-level details while still preserving useful properties of the latent codes.*

## 1. Introduction

The diffusion autoencoder (DAE), proposed in 2022 by Preechakul *et al.*, is a type of latent generative models in which diffusion models are used to both (1) generate latent representations and (2) decode them to full-fledged data items [60]. More specifically, a diffusion autoencoder has three components. The *encoder* is a feed-forward network that encodes an image  $x$  into a 1D vector  $z$  called a *latent code*.<sup>1</sup> The *decoder* is a conditional diffusion model [22, 66] tasked with reconstructing  $x$  given  $z$  through the diffusion process. The *latent code model*<sup>2</sup> is an unconditional diffusion model trained to sample  $z$  from its distribution. Preechakul *et al.* show that DAEs can learn latent codes that can be manipulated to yield meaningful

changes in the image space and interpolated to produce smooth transitions similar to those produced by GANs [18] and VAEs [40]. Because of these capabilities, DAEs have been used or extended for numerous tasks and domains, including facial image generation [37, 71], facial image manipulation [5, 7, 8, 13, 15, 30, 36, 48, 75], medical imaging [20, 29, 35], security [2–4, 50], visual counterfactual explanation generation [42, 65], 3D content generation [24, 76, 87], and image compression [82].

Despite DAEs’ popularity, we only found few studies that optimize their model architecture and hyperparameters [26, 82]. On the contrary, there are many such studies on vanilla diffusion models [9, 10, 12, 23, 33, 34, 54, 59]. As a result, how to best implement a DAE is still not well understood. More specifically, DAE is still largely stuck in the way diffusion models were implemented in 2020: the decoder is trained to predict noise under the “linear- $\beta$ ” schedule [22, 60]. However, there are now two alternative prediction types [63, 67] and several other noise schedules [6, 23, 26, 54, 70].

We show that the original implementation above can be significantly improved in terms of image reconstruction quality. We propose a new method for training DAEs without changing the architecture. It improves image reconstruction quality over the baseline [60] while preserving the interpretability, interpolability, and manipulability of the latent codes.

Our method consists of three parts. First, we change the noise schedule from the linear- $\beta$  schedule to one that have more sampling steps in the low-noise region [23], hoping that the DAE would produce sharper and more accurate details. Second, we change what the model predicts from noise to velocity [63], as we discovered that noise prediction does not work with the new noise schedule. These two changes together produce a model with improved details but worsen overall image similarity. Third, we split training into two phases. In the first phase, the input is always pure Gaussian noise, so the model is trained as a vanilla autoencoder. In the second phase, the model is trained as a DAE using the proposed noise schedule. The two-phase algorithm makes the model a much better autoencoder that

<sup>1</sup>The original paper calls this the “semantic subcode.”

<sup>2</sup>The original paper calls this the “latent DDIM.”

yields more faithful reconstruction of both details and large-scale structures.

## 2. Related Works

Many generative models are *latent variable models* whose process of generating a data item  $\mathbf{x}$  involves first generating a *latent code*  $\mathbf{z}$  in a separate space and then sampling  $\mathbf{x}$  conditioned on  $\mathbf{z}$ . In image generation context, there are two main types of latent codes. An *image-like latent code* is a smaller image whose pixels are feature vectors. As a result, the composition of  $\mathbf{x}$  can be encoded by simply placing the right feature at the right pixel. Spatial latent codes are mainly used to speed up the generation process [17, 61]. A *vector latent code* is a 1D vector with no spatial extent. They are employed by GANs and VAEs, and researchers have found that these codes can be interpolated [18] and manipulated [93] to yield high-level changes to images. Moreover, they also provide image representations that can be used for other downstream tasks.

Diffusion models are a class of generative models introduced by Sohl-Dickstein *et al.* in 2015 [66] and popularized by Ho *et al.* in 2020 [22]. Compared to GANs, the SOTA generative model at the time, diffusion models are much easier to train and soon become better at image generation [12]. Diffusion models do not have vector latent codes (though something functionally similar can be extracted [44]). However, there are many ways vector latent codes can interact with diffusion models. Diffusion models can sample vector latent codes that are later decoded by other types of generative models [46, 61, 73], or they can enhance images generated by other latent code models [56]. The lack of “native” vector latent codes makes it harder to perform semantic image manipulation and representation learning in the sense that existing latent code manipulation techniques [28, 81, 93] would no longer apply. It is thus interesting to ask whether one can design a diffusion model with them.

DAE is perhaps the simplest of such a design. It is an autoencoder whose encoder produces a 1D vector and whose decoder is a diffusion model that takes the vector as a conditioning signal [60] through adaptive normalization layers [25]. It can perform many tasks mentioned in the introduction, and its design has been modified in multiple directions. These include creating a DAE from a pretrained vanilla diffusion model [91], extending the encoder [45, 53], adding more structures to vector latent codes [52, 83, 86], introducing new losses [27, 31, 77] and so on [38, 77, 80, 84]. Our work does not change DAE’s design but gives a new training method that improves image reconstruction.

The closest work to ours is by Yang and Mandt in which they study how DAEs can be used for image compression [82] and so focus on reconstruction quality. Nevertheless, their latent code produced by the encoder is actually image-

like, and they do not evaluate whether it can still be interpolated or manipulated. Another closely related work is by Hudson *et al.*, which, like ours, proposes a new way to train DAEs [26]. The authors introduce a new noise schedule and make the decoder perform view synthesis instead of reconstruction. In contrast, our work uses a different noise schedule and does not change what a DAE does. We evaluated Hudson *et al.*’s training setup without incorporating view synthesis.

For brevity, we shall refer to “vector latent code as” as just “latent code” from now on.

## 3. Background

We represent an image with a real vector  $\mathbf{x} \in \mathbb{R}^D$ , and let  $p_{\text{data}}$  denote the distribution of images. Following Kingma *et al.* [41], we define a stochastic process  $\{\mathbf{x}_t : t \in [0, 1]\}$  such that  $\mathbf{x}_0 \sim p_{\text{data}}$  and  $\mathbf{x}_t \sim \mathcal{N}(\alpha_t \mathbf{x}_0, \sigma_t^2 \mathbf{I})$  for all  $0 \leq t \leq 1$ . We may write  $\mathbf{x}_t = \alpha_t \mathbf{x}_0 + \sigma_t \boldsymbol{\varepsilon}$ , where  $\boldsymbol{\varepsilon} \sim \mathcal{N}(\mathbf{0}, \mathbf{I})$ . The scalar functions  $\alpha_t$  and  $\sigma_t$  are collectively known as the *noise schedule*. In this paper, we use the *variance preserving* formulation [69], where we require that  $\alpha_0 = 1$ ,  $\alpha_1 = 0$ , and  $\alpha_t^2 + \sigma_t^2 = 1$  for all  $t$ , so the noise schedule is defined by  $\alpha_t$  alone. We can show that  $E[\mathbf{x}_0 | \mathbf{x}_t] = (\mathbf{x}_t + \sigma_t^2 \nabla \log p_t(\mathbf{x}_t)) / \alpha_t$ , where  $p_t(\cdot)$  denotes the probability density of  $\mathbf{x}_t$  [16]. The quantity  $\nabla \log p_t(\mathbf{x}_t)$  is called the *score* [68].

**Formulation and training.** A diffusion model is a neural network  $\mathbf{f}_\theta$  such that  $\mathbf{f}_\theta(\mathbf{x}_t, t)$  can be used to estimate the score. The original formulation [22, 66] predicts the Gaussian noise  $\boldsymbol{\varepsilon}$  used to create  $\mathbf{x}_t$  from  $\mathbf{x}_0$ . After the model is trained well, we have that  $\nabla \log p_t(\mathbf{x}_t) \approx -\mathbf{f}_\theta(\mathbf{x}_t, t) / \sigma_t$ . We call this type of model a *noise prediction* or a  $\varepsilon$ -*prediction* model. Song *et al.* observe that one can also train the model to predict  $\mathbf{x}_0$ , which gives  $\nabla \log p_t(\mathbf{x}_t) \approx (\alpha_t \mathbf{f}_\theta(\mathbf{x}_t, t) - \mathbf{x}_t) / \sigma_t^2$  [67]. We call this type of model an *x-prediction model*. Lastly, Salimans and Ho propose the *v-prediction model* where the model is trained to predict the *velocity*  $\mathbf{v}_t := \alpha_t \boldsymbol{\varepsilon} - \sigma_t \mathbf{x}_0$ , which gives  $\nabla \log p_t(\mathbf{x}_t) \approx -\mathbf{x}_t - \alpha_t \mathbf{f}_\theta(\mathbf{x}_t, t) / \sigma_t$  [63].

**Sampling.** Using a trained diffusion model, we can generate a data sample by starting from a Gaussian noise sample and gradually transforming it. There are many algorithms to do so [14, 22, 33, 47, 51, 69, 72, 88, 89, 92], but we rely on a simple algorithm called *DDIM sampling* [67]. We fix  $K + 1$  timesteps  $0 \lesssim t_0 < t_1 < \dots < t_K \lesssim 1$ . Then, we start by sampling  $\mathbf{x}_{t_K} \sim \mathcal{N}(\mathbf{0}, \mathbf{I})$ . Once we have  $\mathbf{x}_{t_k}$  for some  $k$ , we can compute

$$\mathbf{x}_{t_{k-1}} := \frac{\alpha_{t_{k-1}} \mathbf{x}_t + (\alpha_{t_{k-1}} \sigma_{t_k}^2 - \sigma_{t_{k-1}} \sigma_{t_k}) \nabla \log p_t(\mathbf{x}_t)}{\alpha_{t_k}},$$

and repeat this step until we reach  $\mathbf{x}_{t_0}$ , which we output. The score  $\nabla \log p_t(\mathbf{x}_t)$  needs to be replaced with the ap-

proper approximation according to the model’s prediction type.

**Diffusion autoencoder.** A DAE has an encoder  $E$ , a feed-forward neural network which computes a latent code from an input image:  $\mathbf{z} = E(\mathbf{x})$ . The decoder is a conditional diffusion model  $D(\mathbf{x}_t, t, \mathbf{z})$ , which receives  $\mathbf{z}$  as an extra input. Preechakul *et al.* formulate it as an  $\varepsilon$ -prediction model, but we can make it predict either  $x$  or  $v$  too. Applying DDIM sampling to  $D$  with  $\mathbf{z} = E(\mathbf{x})$  should result in a reconstruction of  $\mathbf{x}$ . However, it is not exact because the initial Gaussian noise  $\mathbf{x}_{t_K}$  can introduce variation to the output. As a result,  $\mathbf{x}_{t_K}$  is considered a part of the image’s encoding and is called the *stochastic subcode*. A more accurate reconstruction can be obtained by computing an  $x_{t_K}$  that is specific to the input image by a process called *DDIM inversion* [67]. Though, we generally prefer a DAE where the reconstruction is as faithful as possible without DDIM inversion because it implies that the latent code contains more information and so can be more useful for other tasks.

**Noise schedules.** Originally,  $\alpha_t$  is defined as a discrete-time function. We fix timesteps  $0 = t_0 < t_1 < \dots < t_K \lesssim 1$  where  $K$  is typically 1000, and let  $\alpha_{t_0} = \alpha_0 = 1$ . We then define a sequence  $(\beta_1, \beta_2, \dots, \beta_K)$  and set  $\alpha_{t_k} = \sqrt{\prod_{j=1}^k (1 - \beta_j)}$ . Ho *et al.* propose the *linear- $\beta$  schedule* where  $\beta_k$  varies linearly from  $10^{-4}$  to 0.02 [22]. Preechakul *et al.* use this schedule to train their encoders and decoders.

Later works define  $\alpha_t$  as a continuous function. Nichol and Dhariwal propose  $\alpha_t \approx \cos(\pi t/2)$ , the *cosine schedule* [54]. Hoogeboom *et al.* propose what we call the *shifted cosine schedules* [23],

$$\alpha_t = \text{SC}(t; S) = \sqrt{\text{sigmoid}(-2 \ln \tan(\pi t/2) + 2 \ln S)},$$

which form a family parameterized by a *scaling factor*  $S$ . Observe that  $\text{SC}(t; 1) = \cos(\pi t/2)$ . We plot some shifted cosine schedules and the linear- $\beta$  schedule in Figure 1. We can see that, as  $S$  increases,  $\text{SC}-S$  spends less time in the high-noise region (i.e., the range of  $t$  where  $\alpha_t$  is low). Hoogeboom *et al.* found that, to train diffusion models for high-resolution images ( $256 \times 256$  or  $512 \times 512$ ), it is better to use  $\alpha_t = \text{SC}(t; 32/d)$ , where  $d$  is the width of the images. Chen *et al.* reports similar findings and also proposes another family of shifted noise schedules based on the sigmoid function [6], but we limit our experiments to the shifted cosine family. For brevity, we will refer to  $\text{SC}(t; S)$  as simply  $\text{SC}-S$  from now on.

Hudson *et al.* propose a new “inverted” noise schedule that they claim to be beneficial to representation learning [26]. Unfortunately, we could not find the exact formula in the paper, but we still evaluated Hudson *et al.*’s training method ( $\varepsilon$ -prediction + inverted schedule) in our context and found that it did not work well. Details can be found in the supplementary material.

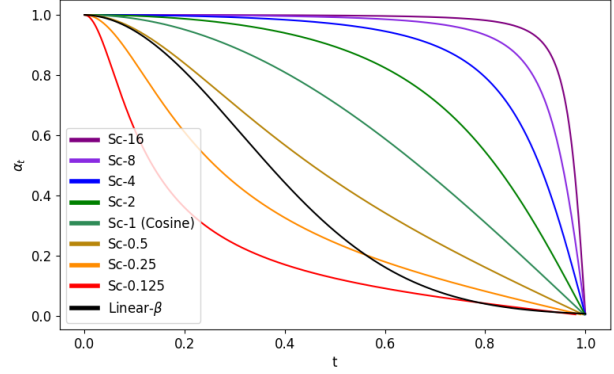


Figure 1. Some noise schedules in the shifted cosine family and the linear- $\beta$  noise schedule.

All the noise schedules we have discussed so far are variance preserving, but there are many that do not obey this constraint [33, 69]. We do not use or evaluate them in this paper.

## 4. Method

We propose a new method to train the encoder and decoder of a DAE [60] (not the latent code model).

- Make the decoder predict  $v$  instead of  $\varepsilon$ .
- Divide training into two phases. First, jointly train the encoder and decoder as a vanilla autoencoder by always sampling  $t = 1$  so that the input image is pure Gaussian noise. Second, train them normally as done in previous work [60], incorporating a noise schedule. In our experiments, the first phase lasts one-fourth of the whole training session, but we have not optimized for the optimal division.
- The noise schedule used in the second phase should have more sampling steps in the low-noise region. We recommend SC-4 (blue).

Pseudocode can be found in the supplementary material. We derived our method through a series of experiments on the CIFAR-10 dataset [43]. In this section, we discuss these experiments and how they informed our choices.

### 4.1. Motivation and Goal

Preechakul *et al.* report that a DAE can generate high-quality images with fewer sampling steps than what a typical diffusion model needs [60].<sup>3</sup> The reason is that the latent code  $\mathbf{z}$ , as an input, helps the decoder to denoise better. Preechakul *et al.* also show that the latent code captures high-level structures while the stochastic subcode captures low-level details.

Based on the above findings, the linear- $\beta$  noise schedule (black) that Preechakul *et al.* use may be suboptimal. During

<sup>3</sup>In particular, see Section 5.5 and Figure 6 in the paper.

the sampling process, high-level structures are recovered in timesteps with high noise levels, while low-level details are refined in those with low noise levels. The schedule allocates most of its timesteps in the high-noise region. As a result, the process would waste timesteps recovering information already present in the latent code instead of generating details. We thus hypothesize that *training a DAE with a noise schedule that spends more time in the low-noise region, such as SC-S with  $S \geq 1$  (i.e.,  $\curvearrowleft$ ,  $\curvearrowright$ ,  $\curvearrowleft$ , or  $\curvearrowright$ ), would yield better images.*

We now elaborate on what “better images” are. As DAE’s main use is manipulating *existing* images through semantic code manipulation and reconstruction, we limit our work to improving its ability to reconstruct rather than to sample new random ones, as in unconditional sampling. There are two methods to reconstruct an image with a DAE. In *stochastic autoencoding*, we encode an input image to a latent code, then sample a random stochastic subcode, and feed both to the decoder. An *inversion* is the same process, but the stochastic subcode is computed with DDIM inversion. We aim to improve both methods but first focus on stochastic autoencoding. Later, we will demonstrate that doing so also enhances inversion.

Among many choices for reconstruction quality metrics (at least 16 [82]), we use the following four, commonly used in previous works [26, 52, 60]: Peak Signal-to-Noise Ratio (PSNR), Structural Similarity Index Measure (SSIM) [78], Learned Perceptual Image Patch Similarity (LPIPS) [90], and Fréchet Inception Distance (FID) [21].<sup>4</sup> The first three metrics measure similarity between original and reconstructed images on a pair-by-pair basis but may fail in measuring sharpness and texture similarity. On the other hand, FID measures these aspects well by comparing the distributions of the original and reconstructed images [26].<sup>5</sup> However, it completely ignores the direct similarity between the original and the reconstruction (Figure 2). Thus, we found it necessary to use all four metrics together.

We generate images with DDIM sampling, and the number of sampling steps can affect the metrics: FID improves significantly when we increase the step count. Nevertheless, more steps mean a longer sampling time. We fix the number of steps to 50, based on the fact that it is the recommended number of steps for a popular diffusion model, Stable Diffusion [58]. Users in general would be familiar with both the time required and the quality afforded by this particular step count.

<sup>4</sup>FID values depend much on implementation details. We record those computed by two widely used libraries: `torch-fidelity` [55] and `clean-fid` [57].

<sup>5</sup>Hudson *et al.* report that the FID captures sharpness and “realism.” However, we found the concept of realism to be vague and decided to replace it with “texture similarity,” which means “similarity of details.”

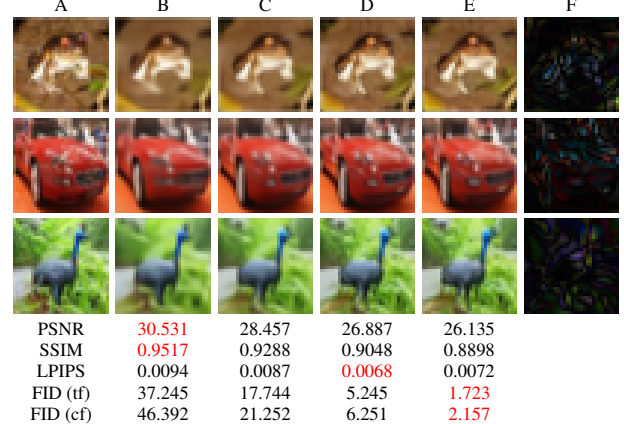


Figure 2. Some (A) CIFAR-10 images and their reconstructions by (B) a vanilla autoencoder trained to minimize the L2 loss, (C) stochastic autoencoding with a DAE with 10 DDIM sampling steps, and (D) stochastic autoencoding with the same DAE at 50 steps and (E) 1000 steps. We show (F) the absolute pixel differences between (D) and (E) to highlight the subtle differences between them. We also show the FID (computed by the `torch-fidelity` (tf) library [55] and the `clean-fid` (cf) library [57] in that order) and averaged PSNR, SSIM, and LPIPS values computed from the reconstructions against the dataset. We can see that PNSR and SSIM overly award blurry images (Column B and C). LPIPS does not fall for the same trap but scores the sharpest (as measured by FID) reconstructions at 1000 steps worse than those at 50 steps. The FID, on the other hand, does not measure alignment between the reconstructed and the original, so it scores the most structurally accurate images in Column B the worst.

## 4.2. Problems with Noise Prediction

The simplest modification to Preechakul *et al.*’s training method is to change the linear- $\beta$  schedule ( $\curvearrowright$ ) to one that spends more time in the low-noise region. Nevertheless, we learned through an experiment that an  $\varepsilon$ -prediction model does not work well with such a noise schedule. In the experiment, we chose SC-4 ( $\curvearrowright$ ) as a representative and trained three DAEs, which predict  $\varepsilon$ ,  $x$ , and  $v$ , for 32M examples (640 epochs). The size of the latent code is 512, following the original paper [60]. Other training details can be found in the supplementary material. We report metrics of reconstructions obtained by stochastic autoencoding in Table 1, which shows that the  $\varepsilon$ -prediction model performs poorly on the three image similarity metrics. It cannot autoencode many images accurately, as can be seen in Figure 3, and so is not usable. On the other hand, the  $x$ -prediction and  $v$ -prediction models are still viable.

The DAE’s encoder and decoder must learn to autoencode images together. We first note that using a noise schedule such as SC-4 ( $\curvearrowright$ ) makes this task harder for all models. When the noise level is low, almost all the information

Prediction type	PSNR↑	SSIM↑	LPIPS↓	FID↓ (tf)	FID↓ (cf)
$\varepsilon$ -prediction	15.534	0.4954	0.0373	4.7651	5.1589
$x$ -prediction	27.147	0.9075	0.0065	3.9349	5.8098
$v$ -prediction	23.664	0.8237	0.0116	1.8133	2.1323

Table 1. Quality of CIFAR-10 images reconstructed by DAEs trained on the SC-4 schedule.



Figure 3. Some (A) original CIFAR-10 images and their reconstruction by the (B)  $\varepsilon$ -predicting, (C)  $x$ -predicting, and (D)  $v$ -predicting DAEs in Table 1. The  $\varepsilon$ -predicting DAE simply fails at being an accurate autoencoder.

about the original image is already present in the decoder’s noised input, reducing the need to utilize the encoder’s output. As a result, the encoder and decoder have fewer opportunities to learn to cooperate under a noise schedule that spends more time in the low-noise region. That fact the  $\varepsilon$ -prediction model becomes unusable suggests that it struggles to learn how to autoencode more than the other two. This might be due to the fact that, at high noise levels, an  $\varepsilon$ -predicting decoder is asked to output something already similar to the noised input, so there is little pressure for the encoder and decoder to learn to cooperate during training.

While an  $\varepsilon$ -prediction model can become usable if we use schedules that spend more time in the high-noise region, such as SC-2 (green) or SC-1 (red), we decided to rule out formulating a DAE with  $\varepsilon$ -prediction when we try other schedules from the shifted cosine family in order to limit resources we use in further experiments.

### 4.3. Impact of Noise Schedules

With the prediction types narrowed down, we next identify the best noise schedule. We trained 10 DAEs using prediction types  $x$  and  $v$ , and 5 different schedules (linear- $\beta$  and SC with  $S = 1, 2, 4, 8$ ). Training details are unchanged from the previous section. Table 2 shows the image quality metrics, revealing three trends.

First, when a noise schedule spends less time in the high-noise region (i.e., going from  $\curvearrowleft$  to  $\curvearrowright$ ), the three image similarity metrics worsen.

Second, the FID, on the contrary, improves until it peaks at SC-4 (blue) and then worsens at SC-8 (purple).

Third, for the same noise schedule,  $x$ -prediction generally yields better image similarity scores than  $v$ -prediction but worse FID.

The first trend suggests that autoencoding is easier to learn at high noise levels. The second trend follows from the

Pred	Schedule	PSNR↑	SSIM↑	LPIPS↓	FID↓ (tf)	FID↓ (cf)
$x$	linear- $\beta$ $\curvearrowleft$	30.296	0.9516	0.0038	6.8907	8.4820
$x$	Sc-1 $\curvearrowright$	29.019	0.9369	0.0046	5.0481	7.0456
$x$	Sc-2 $\curvearrowright$	28.245	0.9265	0.0053	4.8375	6.9604
$x$	Sc-4 $\curvearrowright$	27.147	0.9075	0.0065	3.9349	5.8098
$x$	Sc-8 $\curvearrowright$	25.057	0.8596	0.0101	4.4343	6.2864
$v$	linear- $\beta$ $\curvearrowleft$	29.438	0.9437	0.0046	7.7344	9.4366
$v$	Sc-1 $\curvearrowright$	28.626	0.9333	0.0048	4.3175	5.2237
$v$	Sc-2 $\curvearrowright$	27.094	0.9082	0.0064	2.7339	3.3155
$v$	Sc-4 $\curvearrowright$	23.664	0.8237	0.0116	1.8133	2.1323
$v$	Sc-8 $\curvearrowright$	20.842	0.7176	0.0193	2.0235	2.3003

Table 2. Impact of noise schedule and model prediction type on image quality of DAEs trained on CIFAR-10.

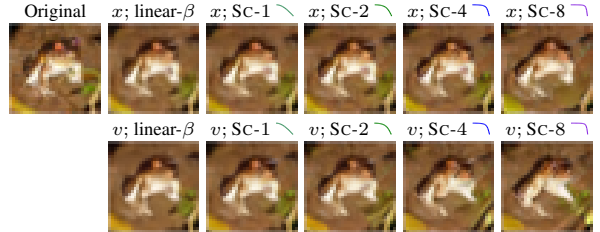


Figure 4. Reconstructions of a frog image from CIFAR-10 by some of the DAEs from Table 2. Notice that the images become sharper and noisier but less accurate as one moves to the right.

fact that the FID is greatly influenced by details, and more time in the low-noise region allows the decoder to perfect the details more. However, spending too much time in the low-noise region can impair the DAE’s autoencoding ability, resulting in image distribution drift and poorer FID. We surmise that this is the case for SC-8 (purple). As evidence, we show reconstructions of a frog image from the data in Figure 4. Notice the reconstruction inaccuracies from SC-8 (purple): the  $x$ -prediction model misses the green blob on the right, and the  $v$ -prediction model misses the frog’s eyes. The last trend is a direct result of model prediction type. Because an  $x$ -prediction model is always asked to recover the original image, it would naturally be better at autoencoding. However, it may not be as effective at recovering details compared to the  $v$ -prediction model due to their training differences. At low-noise levels, which are critical for detail recovery, the noised input already closely resembles the clean input that the  $x$ -prediction model has to predict. Because the prediction requires minimal effort, it provides fewer learning opportunities.

We thought that using a shifted cosine schedule would improve all scores, but instead we discovered a tradeoff. The combination with the best FID ( $v$ -prediction and SC-4  $\curvearrowright$ ) results in poor image similarity scores, while the combination with the best image similarity ( $x$ -prediction and linear- $\beta$   $\curvearrowleft$ ) results in a poor FID.

Phase 1	Phase 2	PSNR↑	SSIM↑	LPIPS↓	FID↓ (tf)	FID↓ (cf)
Sc-4 ↗	N/A	25.955	0.8863	0.0072	1.2566	1.4634
$t = 1$	N/A	30.531	0.9517	0.0094	37.2447	46.3921
$t = 1$	Sc-2 ↗	<b>30.711</b>	<b>0.9580</b>	<b>0.0030</b>	3.2172	4.0042
$t = 1$	Sc-4 ↗	30.351	0.9552	0.0032	<b>2.1149</b>	2.7153
$t = 1$	Sc-8 ↗	28.647	0.9367	0.0050	2.1368	<b>2.6579</b>
$t = 1$	Sc-16 ↗	22.477	0.8176	0.0167	3.4845	4.0712

Table 3. Performance of DAEs trained with 1-phase (first two rows) and 2-phase (last four rows) algorithms using different noise schedules on CIFAR-10. The term  $t = 1$  means that the input is always pure Gaussian noise.

#### 4.4. Two-Phase Training Algorithm

The tradeoff motivated us to seek a solution that improves both reconstruction accuracy and texture similarity simultaneously. Our idea is to start with the combination that yields the best FID score,  $v$ -prediction and Sc-4 (↗), and then modify it to improve reconstruction quality. The main problem with the combo is that the DAE spends too little time in the high-noise region to learn to autoencode.

To fix this, we divide training into two phases, where the DAE is first trained to only autoencode and then trained normally to improve sharpness and texture similarity. The only difference between the two phases is how the time variable,  $t$ , is sampled during training:  $t$  is always set to 1 in the first phase but sampled from  $[0, 1]$  in the second.

To see why the first phase teaches the model to autoencode, recall that when  $t = 1$ , the noisy input  $\mathbf{x}_1$  is a Gaussian noise. Because the decoder is a  $v$ -prediction model, it is asked to predict  $\mathbf{v}_1 = \alpha_1 \epsilon - \sigma_1 \mathbf{x}_0 = -\mathbf{x}_0$ , which is (the negative of) a clean image. Because no information about  $\mathbf{x}_0$  can be conveyed through  $\mathbf{x}_1$ , the encoder is forced to compress that information into the latent code  $\mathbf{z}$  in order to help the decoder do its job. Hence, Phase 1 teaches the system to autoencode.

Unfortunately, because we add a training phase, it becomes unclear whether Sc-4 is still the optimal noise schedule. Those that spend even more time in the low-noise region—Sc-8 (↗) and Sc-16 (↗)—may perform better because the second phase starts with a trained autoencoder.

To validate two-phase training and to find its best noise schedule, we trained a DAE in the first phase for 16M examples (80 epochs). We then trained four DAEs from this starting state for 48M examples (240 epochs) using shifted cosine schedules with  $S = 2 ↗, 4 ↗, 8 ↗$ , and  $16 ↗$ . The metrics are available in Table 3 along with those of a DAE trained normally with Sc-4 (↗) for 64M examples (320 epochs) to match the total training length of other models.

Based on the results above, Sc-4 (↗) seems to yield the best balance between reconstruction accuracy and sharpness/texture similarity, and so it turns out to be the optimal noise schedule for two-phase training as well.

## 5. Results

We evaluated the proposed two-phase training method against the baseline, the training method proposed by Preechakul *et al.* [60], which trains an  $\epsilon$ -prediction model normally with the linear- $\beta$  schedule [60]. We also include results from training a  $v$ -prediction model with Sc-4 (↗) normally to serve as an ablation study. We also experimented with the training method from Hudson *et al.*’s paper ( $\epsilon$ -prediction model with the “inverted” schedule) [26], but we relegate the results to the supplementary material, as we found that it did not produce a usable autoencoder.

### 5.1. Image Reconstruction

We trained DAEs on 4 datasets: CIFAR-10 at image resolution  $32 \times 32$ , CelebA [49] at  $64 \times 64$ , LSUN Bedroom [85] at  $128 \times 128$ , and ImageNet [11] at  $32 \times 32$ . As stated earlier, the first phase of the two-phase training algorithm takes one fourth of the total training length, and the training lengths for models on the same dataset are identical. Model and training details can be found in the supplementary material.

For each datasets, we used the DAEs to reconstruct 50,000 images with both stochastic autoencoding and inversion as discussed in Section 4.1. DDIM sampling and DDIM inversion both use 50 steps. Metrics are available in Table 4. We can see that our method always yield the best image similarity metrics and sometimes the best FID scores. Even when its FID scores are lower than those of the 1-phase training algorithm, the differences are minimal. Moreover, all of our metrics are better than those of Preechakul *et al.*’s training method. The 1-phase training algorithm yielded the best FID scores most of the time, but its other metrics are worse than the baseline. This shows that the 2-phase training method yields both reconstruction accuracy and texture similarity.

We show some of the reconstructions from the CelebA and ImageNet datasets in Figure 5. Notice that the faces reconstructed by the DAE trained with the baseline method are blurrier than those reconstructed by other methods. The soccer ball images confirm that our two-phase training method yields much more accurate stochastic autoencoding than the comparisons. Additionally, we show images reconstructed by stochastic autoencoding from the LSUN Bedroom dataset in Figure 6, and they further demonstrate that our method preserves image structures better than others. More results are available in the supplementary material.

### 5.2. Properties of Latent Codes

We now show that the latent codes produced by our training method still retain the useful properties typically associated with DAE latent codes. Due to space constraints, more results are in the supplementary material.

**Interpolability.** In Figure 7, we show images generated by spherical linear interpolation (slerp) of the semantic and

Dataset	Method	Stochastic decoding						Inversion					
		PSNR↑	SSIM↑	LPIPS↓	FID↓ (tf)	FID↓ (cf)	PSNR↑	SSIM↑	LPIPS↓	FID↓ (tf)	FID↓ (cf)		
CIFAR-10 32	Preechakul <i>et al.</i>	26.887	0.9048	0.006787	5.2448	6.2506	35.667	0.9834	0.002249	11.4542	14.8504		
	1-phase; Sc-4 ↗	25.955	0.8863	0.007197	1.2566	1.4634	49.510	0.9995	0.000071	0.5434	0.6872		
	2-phase; Sc-4 ↗	30.351	0.9552	0.003217	2.1149	2.7153	50.113	0.9996	0.000044	0.7560	0.9032		
CelebA 64	Preechakul <i>et al.</i>	23.974	0.8186	0.030239	11.3050	14.3548	35.929	0.9744	0.008320	15.0237	19.5310		
	1-phase; Sc-4 ↗	23.943	0.8160	0.025720	1.8559	2.2449	45.969	0.9978	0.000766	1.2281	1.6972		
	2-phase; Sc-4 ↗	26.122	0.8696	0.021513	2.3592	2.9030	47.646	0.9982	0.000700	1.5277	2.1107		
Bedroom 128	Preechakul <i>et al.</i>	16.120	0.4051	0.282071	28.8706	26.2747	29.039	0.8932	0.102119	16.8510	17.9375		
	1-phase; Sc-4 ↗	17.964	0.4757	0.268361	3.3717	3.9362	30.412	0.9457	0.056554	1.6781	2.3033		
	2-phase; Sc-4 ↗	20.309	0.5982	0.183325	3.2151	3.9847	37.268	0.9850	0.014716	1.1632	2.0454		
ImageNet 32	Preechakul <i>et al.</i>	21.168	0.7146	0.017876	12.4695	13.6909	34.794	0.9811	0.003229	8.8971	11.5388		
	1-phase; Sc-4 ↗	20.708	0.6979	0.018849	8.5026	9.4456	45.444	0.9985	0.000183	0.5794	0.7365		
	2-phase; Sc-4 ↗	27.811	0.9210	0.005147	4.1131	5.5029	48.892	0.9994	0.000045	0.6588	0.8226		

Table 4. Comparison of image reconstruction performance of the proposed training method with baselines.

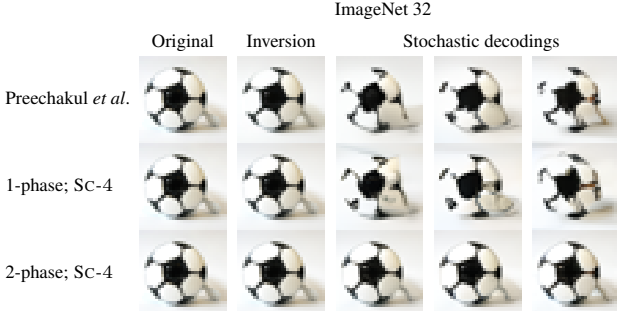
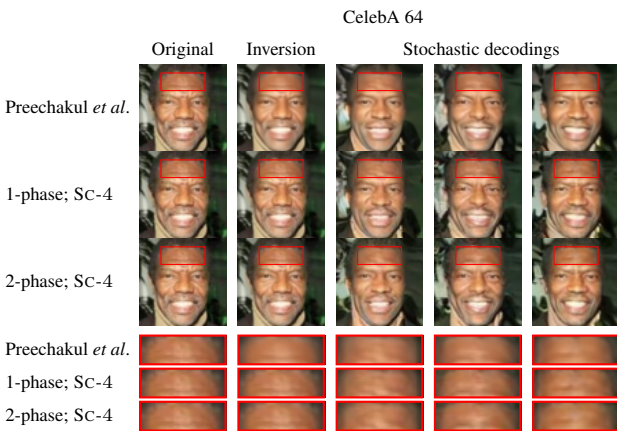


Figure 5. Image reconstruction on CelebA and ImageNet datasets.

stochastic subcodes of image pairs. We can see that the in-betweens produced by the three training methods are similar in terms of difference between adjacent images, showing that our latent codes still retain interpolability. To quantify how smooth the interpolation was, we computed the perceptual path length (PPL) metrics [32] of 200 pairs of images from the four datasets and report their values in Table 5. Our method achieves the lowest PPLs, indicating the smoothest interpolation.

**Information within latent codes.** We evaluated how

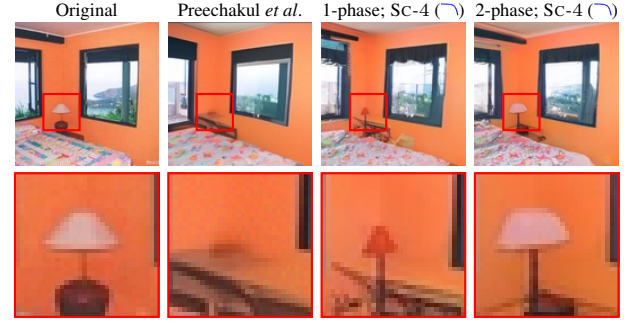


Figure 6. Stochastic decodings of an image from the LSUN Bedroom dataset. The red bounding boxes indicate the most obvious differences between the three models.

Method	CIFAR-10	CelebA	Bedroom	ImageNet
Preechakul <i>et al.</i>	159.52	383.98	770.44	151.19
1-phase; Sc-4 ↗	179.24	378.77	484.17	164.54
2-phase; Sc-4 ↗	155.39	362.61	438.73	146.87

Table 5. Average perceptual path length (PPL)↓ between 200 image pairs. We created 101 in-betweens for each pair with DAEs trained using different methods. The PPLs were computed using the Euler method. See the supplementary for more details.

much information latent codes contain with *linear classifier probes* [1]: we train a linear classifier on the codes and measure its performance. We trained individual classifiers to predict each of the 40 face attributes that come with CelebA and used the area under receiver operating characteristic curve (AUROC) as metric. The macro averages over the attributes of the AUROC for Preechakul *et al.*'s method, the 1-phase training method, and the proposed 2-phase training method are 0.9263, 0.9254, and 0.9195, respectively. The AUROC values for individual properties are available in the supplementary material. While our proposed method came last, our score is only 0.0068 or 0.73% below the best base-



Figure 7. Images generated by interpolating the latent codes and stochastic subcodes of pairs of images and then decoding with some of the DAEs in Section 5.1.

line, suggesting that much information is still retained in our latent codes.

We also trained multi-class linear classifiers to predict CIFAR-10 class membership using the negative log-likelihood loss on softmax logits computed from the latent codes. We tested them on latent codes of the CIFAR-10 test set. The accuracies of the three methods (Preechakul *et al.*, 1-phase training with SC-4  $\curvearrowright$ , and 2-phase training) are 72.71%, 70.61%, and 72.27%, and the macro averages of the AUROC values over 10 classes are 0.9624, 0.9579, and 0.9612. While our proposed 2-phase training method did not achieve the best performance, the numbers were close to those of the baselines.

**Attribute manipulation.** Lastly, we show that we can manipulate the latent codes to manipulate semantic attributes of the corresponding images using the same process as in the original DAE paper [60]. Figure 8 shows some of the manipulated images, which demonstrate the desired high-level changes, similar to the results from the original DAE. Details on the manipulation process and more results can be found in the supplementary material.

## 6. Conclusion

We argue that the training method for DAEs proposed in the original paper [60] and used by many subsequent studies is suboptimal: the noise schedule spends too many steps in the high-noise region, trying to recover high-level image



Figure 8. Attribute manipulation of CelebA images using DAEs trained by (A) Preechakul *et al.*'s training method [60], (B) the 1-phase training with SC-4  $\curvearrowright$ , and (C) our proposed 2-phase training with SC-4  $\curvearrowright$ .

structures. We surmised that the latent code already contains such information, so the decoder should allocate more steps in the low-noise region to improve details. However, we found that choosing a noise schedule involves a trade-off between details and structures. We thus propose a two-phase training method that makes the DAE learn to accurately autoencode in the first and then perfect the details in the second, improving both aspects simultaneously over the baseline training method. We also show that the resulting latent codes retain the abilities to be interpolated and manipulated, while maintaining similar levels of semantic content to those learned by the original training method.

There are several directions for future work. While we show that SC-4  $\curvearrowright$  leads to improvements on all metrics over the baseline, the shifted cosine family offers an infinite number of noise schedules due to the scaling factor  $S$ 's being a real number, and so SC-4 may be suboptimal. Finding the optimal schedule can depend on the dataset, and image characteristics, such as resolution, may affect the optimal choice, similar to a finding by Hoogeboom *et al.* [23]. Moreover, for the proposed two-phase training method, we have not yet optimized the relative duration of the two phases. How to determine this hyperparameter is an important open question.

## References

[1] Guillaume Alain and Yoshua Bengio. Understanding intermediate layers using linear classifier probes, 2018. [7](#)

[2] Zander W. Blasingame and Chen Liu. Leveraging diffusion for strong and high quality face morphing attacks. *IEEE Transactions on Biometrics, Behavior, and Identity Science*, 6(1):118–131, 2024. [1](#)

[3] Zander W. Blasingame and Chen Liu. Fast-dim: Towards fast diffusion morphs, 2024.

[4] Zander W. Blasingame and Chen Liu. Greedy-dim: Greedy algorithms for unreasonably effective face morphs, 2024. [1](#)

[5] Stella Bounareli, Christos Tzelepis, Vasileios Argyriou, Ioannis Patras, and Georgios Tzimiropoulos. Diffusionact: Controllable diffusion autoencoder for one-shot face reenactment. 2024. [1](#)

[6] Ting Chen. On the importance of noise scheduling for diffusion models, 2023. [1, 3](#)

[7] Hansam Cho, Jonghyun Lee, Seunggyu Chang, and Yonghyun Jeong. One-shot structure-aware stylized image synthesis, 2024. [1](#)

[8] Wonwoong Cho, Hareesh Ravi, Midhun Harikumar, Vinh Khuc, Krishna Kumar Singh, Jingwan Lu, David I. Inouye, and Ajinkya Kale. Towards enhanced controllability of diffusion models, 2023. [1](#)

[9] Jooyoung Choi, Jungbeom Lee, Chaehun Shin, Sungwon Kim, Hyunwoo Kim, and Sungroh Yoon. Perception prioritized training of diffusion models. In *IEEE/CVF Conference on Computer Vision and Pattern Recognition, CVPR 2022, New Orleans, LA, USA, June 18-24, 2022*, pages 11462–11471. IEEE, 2022. [1](#)

[10] Katherine Crowson, Stefan Andreas Baumann, Alex Birch, Tanishq Mathew Abraham, Daniel Z. Kaplan, and Enrico Shippole. Scalable high-resolution pixel-space image synthesis with hourglass diffusion transformers, 2024. [1](#)

[11] Jia Deng, Wei Dong, Richard Socher, Li-Jia Li, Kai Li, and Li Fei-Fei. Imagenet: A large-scale hierarchical image database. In *2009 IEEE Conference on Computer Vision and Pattern Recognition*, pages 248–255, 2009. [6](#)

[12] Prafulla Dhariwal and Alexander Nichol. Diffusion models beat gans on image synthesis. In *Advances in Neural Information Processing Systems*, pages 8780–8794. Curran Associates, Inc., 2021. [1, 2](#)

[13] Zheng Ding, Xuaner Zhang, Zhihao Xia, Lars Jebe, Zhuowen Tu, and Xiuming Zhang. Diffusionrig: Learning personalized priors for facial appearance editing. In *CVPR*, 2023. [1](#)

[14] Tim Dernik, Arash Vahdat, and Karsten Kreis. Score-Based Generative Modeling with Critically-Damped Langevin Diffusion. *International Conference on Learning Representations (ICLR)*, 2022. [2](#)

[15] Chenpeng Du, Qi Chen, Tianyu He, Xu Tan, Xie Chen, Kai Yu, Sheng Zhao, and Jiang Bian. Dae-talker: High fidelity speech-driven talking face generation with diffusion autoencoder. In *Proceedings of the 31st ACM International Conference on Multimedia*, page 4281–4289, New York, NY, USA, 2023. Association for Computing Machinery. [1](#)

[16] Bradley Efron. Tweedie’s formula and selection bias. *Journal of the American Statistical Association*, 106:1602 – 1614, 2011. [2](#)

[17] Patrick Esser, Robin Rombach, and Björn Ommer. Taming transformers for high-resolution image synthesis, 2020. [2](#)

[18] Ian Goodfellow, Jean Pouget-Abadie, Mehdi Mirza, Bing Xu, David Warde-Farley, Sherjil Ozair, Aaron Courville, and Yoshua Bengio. Generative adversarial nets. In *Advances in Neural Information Processing Systems*. Curran Associates, Inc., 2014. [1, 2](#)

[19] Kaiming He, Xiangyu Zhang, Shaoqing Ren, and Jian Sun. Deep residual learning for image recognition. In *Proceedings of the IEEE conference on computer vision and pattern recognition*, pages 770–778, 2016. [1](#)

[20] Xiaoxiao He, Chaowei Tan, Ligong Han, Bo Liu, Leon Axel, Kang Li, and Dimitris N. Metaxas. Dmcvr: Morphology-guided diffusion model for 3d cardiac volume reconstruction, 2023. [1](#)

[21] Martin Heusel, Hubert Ramsauer, Thomas Unterthiner, Bernhard Nessler, and Sepp Hochreiter. Gans trained by a two time-scale update rule converge to a local nash equilibrium. In *Advances in Neural Information Processing Systems*. Curran Associates, Inc., 2017. [4](#)

[22] Jonathan Ho, Ajay Jain, and Pieter Abbeel. Denoising diffusion probabilistic models. In *Advances in Neural Information Processing Systems 33: Annual Conference on Neural Information Processing Systems 2020, NeurIPS 2020, December 6-12, 2020, virtual*, 2020. [1, 2, 3](#)

[23] Emiel Hoogeboom, Jonathan Heek, and Tim Salimans. simple diffusion: End-to-end diffusion for high resolution images. In *International Conference on Machine Learning, ICML 2023, 23-29 July 2023, Honolulu, Hawaii, USA*, pages 13213–13232. PMLR, 2023. [1, 3, 8](#)

[24] Jingyu Hu, Ka-Hei Hui, Zhengze Liu, Ruihui Li, and Chi-Wing Fu. Neural wavelet-domain diffusion for 3d shape generation, inversion, and manipulation, 2023. [1](#)

[25] Xun Huang and Serge Belongie. Arbitrary style transfer in real-time with adaptive instance normalization. In *ICCV*, 2017. [2](#)

[26] Drew A. Hudson, Daniel Zoran, Mateusz Malinowski, Andrew K. Lampinen, Andrew Jaegle, James L. McClelland, Loic Matthey, Felix Hill, and Alexander Lerchner. Soda: Bottleneck diffusion models for representation learning, 2023. [1, 2, 3, 4, 6](#)

[27] Jensen Hwa, Qingyu Zhao, Aditya Lahiri, Adnan Masood, Babak Salimi, and Ehsan Adeli. Enforcing conditional independence for fair representation learning and causal image generation. In *Proceedings of the IEEE/CVF Conference on Computer Vision and Pattern Recognition (CVPR) Workshops*, pages 103–112, 2024. [2](#)

[28] Erik Härkönen, Aaron Hertzmann, Jaakko Lehtinen, and Sylvain Paris. Ganspace: Discovering interpretable gan controls. In *Proc. NeurIPS*, 2020. [2](#)

[29] Ayodeji Ijishakin, Sophie Martin, Florence Townend, Federica Agosta, Edoardo Gioele Spinelli, Silvia Basaia, Paride Schito, Yuri Falzone, Massimo Filippi, James Cole, and Andrea Malaspina. Semi-supervised diffusion model for brain age prediction, 2024. [1](#)

[30] Haozhe Jia, Yan Li, Hengfei Cui, Di Xu, Changpeng Yang, Yuwang Wang, and Tao Yu. Discontrolface: Disentangled control for personalized facial image editing, 2023. 1

[31] Xin Jin, Bohan Li, BAAO Xie, Wenya Zhang, Jinming Liu, Ziqiang Li, Tao Yang, and Wenjun Zeng. Closed-loop unsupervised representation disentanglement with  $\beta$ -vae distillation and diffusion probabilistic feedback, 2024. 2

[32] Tero Karras, Samuli Laine, and Timo Aila. A style-based generator architecture for generative adversarial networks. In *2019 IEEE/CVF Conference on Computer Vision and Pattern Recognition (CVPR)*, pages 4396–4405, 2019. 7, 5

[33] Tero Karras, Miika Aittala, Timo Aila, and Samuli Laine. Elucidating the design space of diffusion-based generative models, 2022. 1, 2, 3

[34] Tero Karras, Miika Aittala, Jaakko Lehtinen, Janne Hellsten, Timo Aila, and Samuli Laine. Analyzing and improving the training dynamics of diffusion models, 2023. 1

[35] Matthias Keicher, Matan Atad, David Schinz, Alexandra S. Gersing, Sarah C. Foreman, Sophia S. Goller, Juergen Weissinger, Jon Rischewski, Anna-Sophia Dietrich, Benedikt Wiestler, Jan S. Kirschke, and Nassir Navab. Semantic latent space regression of diffusion autoencoders for vertebral fracture grading, 2023. 1

[36] Gyeongman Kim, Hajin Shim, Hyunsu Kim, Yunjey Choi, Junho Kim, and Eunho Yang. Diffusion video autoencoders: Toward temporally consistent face video editing via disentangled video encoding. In *Proceedings of the IEEE/CVF Conference on Computer Vision and Pattern Recognition (CVPR)*, pages 6091–6100, 2023. 1

[37] Minchul Kim, Feng Liu, Anil Jain, and Xiaoming Liu. Dc-face: Synthetic face generation with dual condition diffusion model. In *Proceedings of the IEEE/CVF Conference on Computer Vision and Pattern Recognition (CVPR)*, pages 12715–12725, 2023. 1

[38] Yeongmin Kim, Kwanghyeon Lee, Minsang Park, Byeongku Na, and Il-Chul Moon. Diffusion bridge autoencoders for unsupervised representation learning, 2024. 2

[39] Diederik P. Kingma and Jimmy Ba. Adam: A method for stochastic optimization, 2014. cite arxiv:1412.6980Comment: Published as a conference paper at the 3rd International Conference for Learning Representations, San Diego, 2015. 2

[40] Diederik P. Kingma and Max Welling. Auto-Encoding Variational Bayes. In *2nd International Conference on Learning Representations, ICLR 2014, Banff, AB, Canada, April 14-16, 2014, Conference Track Proceedings*, 2014. 1

[41] Diederik P. Kingma, Tim Salimans, Ben Poole, and Jonathan Ho. Variational diffusion models, 2021. 2

[42] Aneesh Komanduri, Chen Zhao, Feng Chen, and Xintao Wu. Causal diffusion autoencoders: Toward counterfactual generation via diffusion probabilistic models, 2024. 1

[43] Alex Krizhevsky. Cifar-10 and cifar-100 datasets. <https://www.cs.toronto.edu/~kriz/cifar.html>, 2009. Accessed: 2024-06-12. 3

[44] Mingi Kwon, Jaeseok Jeong, and Youngjung Uh. Diffusion models already have a semantic latent space, 2023. 2

[45] Yipeng Leng, Qiangjuan Huang, Zhiyuan Wang, Yangyang Liu, and Haoyu Zhang. Diffusegae: Controllable and high-fidelity image manipulation from disentangled representation, 2023. 2

[46] Tianhong Li, Dina Katabi, and Kaiming He. Return of unconditional generation: A self-supervised representation generation method, 2024. 2

[47] Luping Liu, Yi Ren, Zhijie Lin, and Zhou Zhao. Pseudo numerical methods for diffusion models on manifolds, 2022. 2

[48] Tao Liu, Chenpeng Du, Shuai Fan, Feilong Chen, and Kai Yu. Diffdub: Person-generic visual dubbing using inpainting renderer with diffusion auto-encoder, 2024. 1

[49] Ziwei Liu, Ping Luo, Xiaogang Wang, and Xiaoou Tang. Deep learning face attributes in the wild. In *Proceedings of International Conference on Computer Vision (ICCV)*, 2015. 6

[50] Min Long, Quantao Yao, Le-Bing Zhang, and Fei Peng. Face de-morphing based on diffusion autoencoders. *IEEE Transactions on Information Forensics and Security*, 19:3051–3063, 2024. 1

[51] Cheng Lu, Yuhao Zhou, Fan Bao, Jianfei Chen, Chongxuan Li, and Jun Zhu. Dpm-solver: A fast ode solver for diffusion probabilistic model sampling in around 10 steps. *arXiv preprint arXiv:2206.00927*, 2022. 2

[52] Zeyu Lu, Chengyue Wu, Xinyuan Chen, Yaohui Wang, Lei Bai, Yu Qiao, and Xihui Liu. Hierarchical diffusion autoencoders and disentangled image manipulation. *CoRR*, abs/2304.11829, 2023. 2, 4

[53] Sarthak Mittal, Korbinian Abstreiter, Stefan Bauer, Bernhard Schölkopf, and Arash Mehrjou. Diffusion based representation learning. In *Proceedings of the 40th International Conference on Machine Learning*, pages 24963–24982. PMLR, 2023. 2

[54] Alex Nichol and Prafulla Dhariwal. Improved denoising diffusion probabilistic models, 2021. 1, 3

[55] Anton Obukhov, Maximilian Seitzer, Po-Wei Wu, Semen Zhydenko, Jonathan Kyl, and Elvis Yu-Jing Lin. High-fidelity performance metrics for generative models in pytorch, 2020. Version: 0.3.0, DOI: 10.5281/zenodo.4957738. 4

[56] Kushagra Pandey, Avideep Mukherjee, Piyush Rai, and Abhishek Kumar. Diffusevae: Efficient, controllable and high-fidelity generation from low-dimensional latents, 2022. 2

[57] Gaurav Parmar, Richard Zhang, and Jun-Yan Zhu. On aliased resizing and surprising subtleties in gan evaluation. In *CVPR*, 2022. 4

[58] Suraj Patil, Pedro Cuenca, Nathan Lambert, and Patrick von Platen. Stable diffusion with diffusers. [https://huggingface.co/blog/stable\\_diffusion](https://huggingface.co/blog/stable_diffusion), 2022. Accessed: 2024-07-02. 4

[59] William Peebles and Saining Xie. Scalable diffusion models with transformers. In *IEEE/CVF International Conference on Computer Vision, ICCV 2023, Paris, France, October 1-6, 2023*, pages 4172–4182. IEEE, 2023. 1

[60] Konpat Preechakul, Nattanat Chathee, Suttisak Wizadwongsu, and Supasorn Suwajanakorn. Diffusion autoencoders: Toward a meaningful and decodable representation.

In *IEEE Conference on Computer Vision and Pattern Recognition (CVPR)*, 2022. 1, 2, 3, 4, 6, 8

[61] Robin Rombach, Andreas Blattmann, Dominik Lorenz, Patrick Esser, and Björn Ommer. High-resolution image synthesis with latent diffusion models. In *Proceedings of the IEEE/CVF Conference on Computer Vision and Pattern Recognition (CVPR)*, pages 10684–10695, 2022. 2

[62] Olaf Ronneberger, Philipp Fischer, and Thomas Brox. U-net: Convolutional networks for biomedical image segmentation. In *Medical Image Computing and Computer-Assisted Intervention (MICCAI)*, pages 234–241. Springer, 2015. (available on arXiv:1505.04597 [cs.CV]). 1

[63] Tim Salimans and Jonathan Ho. Progressive distillation for fast sampling of diffusion models. *CoRR*, abs/2202.00512, 2022. 1, 2

[64] Karen Simonyan and Andrew Zisserman. Very deep convolutional networks for large-scale image recognition. In *Proceedings of the International Conference on Learning Representations (ICLR)*, 2015. 5

[65] Bartłomiej Sobieski and Przemysław Biecek. Global counterfactual directions, 2024. 1

[66] Jascha Sohl-Dickstein, Eric A. Weiss, Niru Maheswaranathan, and Surya Ganguli. Deep unsupervised learning using nonequilibrium thermodynamics. In *Proceedings of the 32nd International Conference on International Conference on Machine Learning - Volume 37*, page 2256–2265. JMLR.org, 2015. 1, 2

[67] Jiaming Song, Chenlin Meng, and Stefano Ermon. Denoising diffusion implicit models, 2020. 1, 2, 3

[68] Yang Song and Stefano Ermon. Generative modeling by estimating gradients of the data distribution. In *Advances in Neural Information Processing Systems*. Curran Associates, Inc., 2019. 2

[69] Yang Song, Jascha Sohl-Dickstein, Diederik P Kingma, Abhishek Kumar, Stefano Ermon, and Ben Poole. Score-based generative modeling through stochastic differential equations. In *International Conference on Learning Representations*, 2021. 2, 3

[70] Yang Song, Prafulla Dhariwal, Mark Chen, and Ilya Sutskever. Consistency models, 2023. 1

[71] Yu-Chuan Su, Kelvin C. K. Chan, Yandong Li, Yang Zhao, Han Zhang, Boqing Gong, Huisheng Wang, and Xuhui Jia. Identity encoder for personalized diffusion, 2023. 1

[72] Hideyuki Tachibana, Mocho Go, Muneyoshi Inahara, Yotaro Katayama, and Yotaro Watanabe. Itô-taylor sampling scheme for denoising diffusion probabilistic models using ideal derivatives. *ArXiv*, abs/2112.13339, 2021. 2

[73] Arash Vahdat, Karsten Kreis, and Jan Kautz. Score-based generative modeling in latent space, 2021. 2

[74] Ashish Vaswani, Noam Shazeer, Niki Parmar, Jakob Uszkoreit, Llion Jones, Aidan N Gomez, Łukasz Kaiser, and Illia Polosukhin. Attention is all you need. In *Advances in Neural Information Processing Systems*. Curran Associates, Inc., 2017. 1

[75] Guangzhi Wang, Tianyi Chen, Kamran Ghasedi, Hsiang-Tao Wu, Tianyu Ding, Chris Nuesmeyer, Ilya Zharkov, Mohan Kankanhalli, and Luming Liang. S3editor: A sparse semantic-disentangled self-training framework for face video editing, 2024. 1

[76] Tengfei Wang, Bo Zhang, Ting Zhang, Shuyang Gu, Jianmin Bao, Tadas Baltrusaitis, Jingjing Shen, Dong Chen, Fang Wen, Qifeng Chen, and Baining Guo. Rodin: A generative model for sculpting 3d digital avatars using diffusion. In *Proceedings of the IEEE/CVF Conference on Computer Vision and Pattern Recognition (CVPR)*, pages 4563–4573, 2023. 1

[77] Yingheng Wang, Yair Schiff, Aaron Gokaslan, Weishen Pan, Fei Wang, Christopher De Sa, and Volodymyr Kuleshov. InfoDiffusion: Representation learning using information maximizing diffusion models. In *Proceedings of the 40th International Conference on Machine Learning*, pages 36336–36354. PMLR, 2023. 2

[78] Zhou Wang, A. C. Bovik, H. R. Sheikh, and E. P. Simoncelli. Image quality assessment: from error visibility to structural similarity. *IEEE Transactions on Image Processing*, 13(4):600–612, 2004. 4

[79] Weilai Xiang. Unofficial implementation for SODA: Bottleneck diffusion models for representation learning. <https://github.com/FutureXiang/soda>, 2023. Accessed: 2024-07-10. 2, 3

[80] Yilun Xu, Gabriele Corso, Tommi Jaakkola, Arash Vahdat, and Karsten Kreis. Disco-diff: Enhancing continuous diffusion models with discrete latents, 2024. 2

[81] Guoxing Yang, Nanyi Fei, Mingyu Ding, Guangzhen Liu, Zhiwu Lu, and Tao Xiang. L2m-gan: Learning to manipulate latent space semantics for facial attribute editing. In *2021 IEEE/CVF Conference on Computer Vision and Pattern Recognition (CVPR)*, pages 2950–2959, 2021. 2

[82] Ruihan Yang and Stephan Mandt. Lossy image compression with conditional diffusion models. In *Advances in Neural Information Processing Systems*, pages 64971–64995. Curran Associates, Inc., 2023. 1, 2, 4

[83] Tao Yang, Yuwang Wang, Yan Lv, and Nanning Zheng. Dis-diff: Unsupervised disentanglement of diffusion probabilistic models, 2023. 2

[84] Tao Yang, Cuiling Lan, Yan Lu, and Nanning zheng. Diffusion model with cross attention as an inductive bias for disentanglement, 2024. 2

[85] Fisher Yu, Yinda Zhang, Shuran Song, Ari Seff, and Jianxiong Xiao. Lsun: Construction of a large-scale image dataset using deep learning with humans in the loop. *arXiv preprint arXiv:1506.03365*, 2015. 6, 2

[86] Zhongqi Yue, Jiankun Wang, Qianru Sun, Lei Ji, Eric I-Chao Chang, and Hanwang Zhang. Exploring diffusion time-steps for unsupervised representation learning, 2024. 2

[87] xiaohui zeng, Arash Vahdat, Francis Williams, Zan Gojcic, Or Litany, Sanja Fidler, and Karsten Kreis. Lion: Latent point diffusion models for 3d shape generation. In *Advances in Neural Information Processing Systems*, pages 10021–10039. Curran Associates, Inc., 2022. 1

[88] Qinsheng Zhang and Yongxin Chen. Fast sampling of diffusion models with exponential integrator. *arXiv preprint arXiv:2204.13902*, 2022. 2

[89] Qinsheng Zhang, Molei Tao, and Yongxin Chen. gddim: Generalized denoising diffusion implicit models, 2022. 2

- [90] Richard Zhang, Phillip Isola, Alexei A. Efros, Eli Shechtman, and Oliver Wang. The unreasonable effectiveness of deep features as a perceptual metric, 2018. [4](#), [5](#)
- [91] Zijian Zhang, Zhou Zhao, and Zhijie Lin. Unsupervised representation learning from pre-trained diffusion probabilistic models, 2023. [2](#)
- [92] Wenliang Zhao, Lujia Bai, Yongming Rao, Jie Zhou, and Jiwen Lu. Unipc: A unified predictor-corrector framework for fast sampling of diffusion models. *arXiv preprint arXiv:2302.04867*, 2023. [2](#)
- [93] Jun-Yan Zhu, Philipp Krähenbühl, Eli Shechtman, and Alexei A. Efros. Generative visual manipulation on the natural image manifold, 2018. [2](#)

# Revisiting Diffusion Autoencoder Training for Image Reconstruction Quality

## Supplementary Material

### 7. Training Algorithms

In this section, we show pseudocode for training diffusion autoencoders. Algorithm 1 trains a diffusion autoencoder as a vanilla autoencoder and is used in the first phase of our proposed method. Algorithm 2 is a generic for training a DAE that works with all types of model prediction:  $\varepsilon$ ,  $x$ , and  $v$ . It is used in the second phase of our method and also used to train baseline models that we compare against. Note that Algorithm 1 is a special case of Algorithm 2 where the decoder is a  $v$ -prediction model, and  $t$  is always set to 1.

---

#### Algorithm 1 Train a diffusion autoencoder as a vanilla encoder

---

```

1: Initialize  $\theta$ , the parameters of the encoder  $E_\theta$  and the decoder  $D_\theta$ .
2: while target training length is not reached do
3:   Sample a data item  $\mathbf{x}_0 \sim p_{\text{data}}$ .
4:    $\mathbf{z} \leftarrow E_\theta(\mathbf{x}_0)$ 
5:   Sample  $\varepsilon \sim \mathcal{N}(0, I)$ .
6:    $\mathbf{y}^* \leftarrow -\mathbf{x}_0$ 
7:    $\mathbf{y} \leftarrow D_\theta(\varepsilon, 1, \mathbf{z})$ 
8:    $\mathcal{L} \leftarrow \|\mathbf{y} - \mathbf{y}^*\|^2$ 
9:   Update  $\theta$  according to the gradient  $\nabla_\theta \mathcal{L}$ .
10: end while

```

---



---

#### Algorithm 2 Train a diffusion autoencoder normally

---

```

1: Initialize  $\theta$ , the parameters of the encoder  $E_\theta$  and the decoder  $D_\theta$ .
2: while target training length is not reached do
3:   Sample a data item  $\mathbf{x}_0 \sim p_{\text{data}}$ .
4:    $\mathbf{z} \leftarrow E_\theta(\mathbf{x}_0)$ 
5:   Sample  $t \sim \mathcal{U}([0, 1])$ .
6:   Sample  $\varepsilon \sim \mathcal{N}(0, I)$ .
7:    $\mathbf{x}_t \leftarrow \alpha_t \mathbf{x}_0 + \sigma_t \varepsilon$ 
8:   if  $D_\theta$  is a  $\varepsilon$ -prediction model then
9:      $\mathbf{y}^* \leftarrow \varepsilon$ 
10:   else if  $D_\theta$  is a  $x$ -prediction model then
11:      $\mathbf{y}^* \leftarrow \mathbf{x}_0$ 
12:   else if  $D_\theta$  is a  $v$ -prediction model then
13:      $\mathbf{y}^* \leftarrow \alpha_t \varepsilon - \sigma_t \mathbf{x}_0$ 
14:   end if
15:    $\mathbf{y} \leftarrow D_\theta(\mathbf{x}_t, t, \mathbf{z})$ 
16:    $\mathcal{L} \leftarrow \|\mathbf{y} - \mathbf{y}^*\|^2$ 
17:   Update  $\theta$  according to the gradient  $\nabla_\theta \mathcal{L}$ .
18: end while

```

---

### 8. Network Architectures and Training Setups

The DAE decoders and encoders are of the architectures used by Preechakul *et al.* [60], which in turn are based on the popular ADM architecture by Dhariwal and Nichol [12]. The size of the latent code is fixed to 512. Each decoder is a U-Net [62] with attention layers [74]. The decoder is conditioned by two pieces of information: the time and the latent code. Each is transformed first by an MLP and then used to modulate, through adaptive group normalization (AdaGN) [12] in ResNet blocks [19], the feature tensor that comes from the input image. Each encoder is the downsampling part of a U-Net with

attention, and it has been configured so that the last output is a 512-component 1D vector. More details can be found in the supplementary material of Preechakul *et al.*’s paper [60]. The DAEs that were trained on the same dataset had the same configuration, and these configurations are shown in Table 6 and Table 7.

Configuration	CIFAR-10 32	CelebA 64	Bedroom 128	ImageNet 32
Base # channel	256	64	128	128
Channel multipliers	[1,1,1]	[1,2,4,8]	[1,1,2,3,4]	[1,2,2,2]
# Resnet blocks per resolution	3	2	2	3
Attention resolutions	[16,8]	[32, 16, 8]	[16]	[16,8]
Dropout probability	0.2	0.1	0.1	0.3
Size (MB)	265	316	427	296

Table 6. ADM configurations of the decoders.

Configuration	CIFAR-10 32	CelebA 64	Bedroom 128	ImageNet 32
Base # channel	128	128	128	128
Channel multipliers	[1,2,4,8]	[1,2,4,8]	[1,1,2,3,4,4]	[1,2,4,8]
# Resnet blocks per resolution	2	2	2	2
Attention resolutions	[16,8,4]	[16,8,4]	[16]	[16, 8, 4]
Dropout probability	0.0	0.0	0.0	0.0
Size (MB)	224	224	96	224

Table 7. ADM configurations of the encoders.

Hyperparameter	CIFAR-10 32	CelebA 64	Bedroom 128	ImageNet 32
Batch size	256	192	96	128
Training length (# examples)	64M	32M	32M	64M
Warm-up length (# examples)	128K	128K	5,120	128K

Table 8. Hyperparameters used for training of DAEs in Section 5 of the main paper.

All DAEs in the main paper were trained with the Adam optimizer [39] with  $\beta_1 = 0.9$  and  $\beta_2 = 0.999$ . The learning rate had a warm-up period where it increased linearly until it reached the maximum value of  $10^{-4}$  and then remained unchanged. The warm-up period is 128,000 training examples for all datasets except LSUN Bedroom [85], for which it was 5 120 training examples. During training, running averages of the models parameters are computed with the exponential moving average (EMA) algorithm with decay of 0.9999, the same as what was done by Ho *et al.* [22]. The time step  $t$  is sampled uniformly from the interval  $[0, 1]$ . We always used models with EMA parameters for evaluation. Other hyperparameters such as the batch size and the training length vary from dataset to dataset. We list those used in Section 5 in Table 8. For the two-phase training algorithm, the first phase took 1/4 of the training length, and the second-phase took the rest. This means that all DAEs were shown the same number of training examples during training. The DAEs in Section 4 uses mostly the same hyperparameters as those in Section 5, but some DAEs were trained for 32M examples instead of 64M examples.

## 9. Evaluation of Hudson *et al.*’s Training Method

Hudson *et al.* proposes a new noise schedule they call the “inverted” schedule [26]. However, the schedule is only depicted in a figure. We could not find any mathematical expression for it inside the paper or the supplementary material, and there is no official code release at the time of writing of our paper. To make progress, we relied on an unofficial implementation by Xiang [79]. Inspecting the code, we deduced that the formula for the inverted schedule was

$$\bar{\alpha}_t = \alpha_t^2 = \frac{2}{\pi} \cos^{-1}(\sqrt{t}),$$

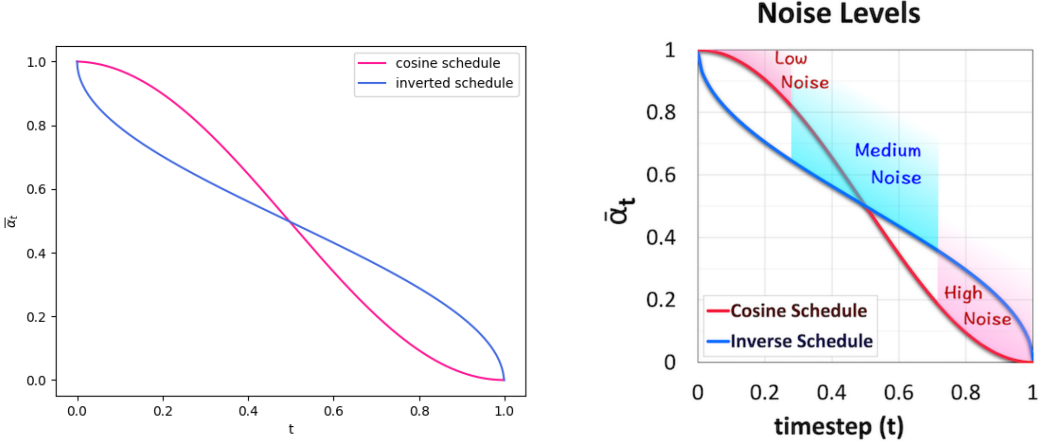


Figure 9. To the left is our reconstruction of Hudson *et al.*’s inverted noise schedule. We show it with the cosine schedule,  $\bar{\alpha}_t = \alpha_t^2 = \cos^2(\pi t/2)$ , so that the plot has the same composition as left plot in Figure 3 of Hudson *et al.*’s paper (reproduced on the right). We found good agreement between the plots, and so we think the formula that we extracted from Xiang’s code [79] is right.

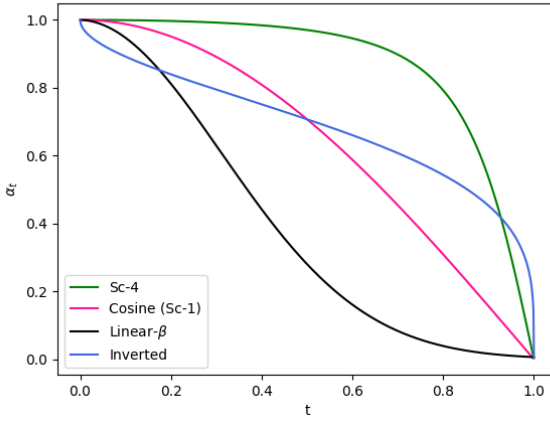


Figure 10. Comparison of Hudson *et al.*’s inverted noise schedule against the linear- $\beta$ , the cosine, and the SC-4 schedules.

which gives

$$\alpha_t = \sqrt{\frac{2}{\pi} \cos^{-1}(\sqrt{t})}.$$

To verify the formula, we plot the schedule with the cosine schedule and show the result in Figure 9. The plot looks like the relevant plot in Hudson *et al.*’s paper, so the formula seems to be correct.

To put the inverted noise schedule in context, we plot its  $\alpha_t$  function (not the  $\bar{\alpha}_t$  function that is depicted in Figure 9) together with those of the linear- $\beta$  schedule, the cosine schedule (which is SC-1), and the SC-4 schedule in Figure 10. We can see that it indeed spends most of its time in the medium noise level, and it even spends less time in the high noise region than SC-4.

Now that we have identified Hudson *et al.*’s noise schedule, we also need to identify the prediction type that they use. This is not stated explicitly anywhere in the paper. However, on Page 4, the authors wrote “[. . .] we extrapolated the model’s output in the conditional direction:  $\varepsilon_\theta(\mathbf{x}_t|\mathbf{z}) - \varepsilon_\theta(\mathbf{x}_t|\mathbf{0})\varepsilon$ ” led us to believe that Hudson *et al.* used the  $\varepsilon$ -prediction model.

We evaluated Hudson *et al.*’s training method ( $\varepsilon$ -prediction with the inverted noise schedule) by training a DAE for each of the 4 datasets we used. We reported metrics for quality of images reconstructed by stochastic autoencoding (no inversion) in

Dataset	Method	Stochastic autoencoding				
		PSNR $\uparrow$	SSIM $\uparrow$	LPIPS $\downarrow$	FID $\downarrow$ (tf)	FID $\downarrow$ (cf)
CIFAR-10 32	Preechakul <i>et al.</i> ( $\varepsilon + \curvearrowright$ )	26.887	0.9048	0.006787	5.2448	6.2506
	2-phase; Sc-4 ( $v + \curvearrowright$ )	30.351	0.9552	0.003217	2.1149	2.7153
	Hudson <i>et al.</i> ( $\varepsilon + \curvearrowright$ )	3.834	-0.1038	0.235412	117.0716	130.0356
CelebA 64	Preechakul <i>et al.</i> ( $\varepsilon + \curvearrowright$ )	23.974	0.8186	0.030239	11.3050	14.3548
	2-phase; Sc-4 ( $v + \curvearrowright$ )	26.122	0.8696	0.021513	2.3592	2.9030
	Hudson <i>et al.</i> ( $\varepsilon + \curvearrowright$ )	10.985	0.3069	0.328190	163.6320	190.6296
Bedroom 128	Preechakul <i>et al.</i> ( $\varepsilon + \curvearrowright$ )	16.120	0.4051	0.282071	28.8706	26.2747
	2-phase; Sc-4 ( $v + \curvearrowright$ )	20.309	0.5982	0.183325	3.2151	3.9847
	Hudson <i>et al.</i> ( $\varepsilon + \curvearrowright$ )	7.709	0.1615	0.652557	276.7475	280.5181
ImageNet 32	Preechakul <i>et al.</i> ( $\varepsilon + \curvearrowright$ )	21.168	0.7146	0.017876	12.4695	13.6909
	2-phase; Sc-4 ( $v + \curvearrowright$ )	27.811	0.9210	0.005147	4.1131	5.5029
	Hudson <i>et al.</i> ( $\varepsilon + \curvearrowright$ )	12.983	0.4536	0.070556	71.7630	91.9553

Table 9. Comparison of stochastic autoencoding performance of the baseline, our proposed method, and Hudson *et al.*’s training method.

Table 9. We can see that the numbers are particular bad. The PSNR values are very low, which means that the reconstructions are not accurate at all. We can see when we look at some of the reconstructed images in Figure 11. Observe that the colors of the images reconstructed by the DAEs trained with Hudson *et al.*’s method are wrong.

We were very surprised by the results because we expected that at least the colors would be correct. We checked our code for bugs but, to the best of our ability, could not find any. (We used the same code to train other DAEs, and we changed only the noise schedule to accommodate Hudson *et al.*’s setting.) We surmise that the DAE’s inability to autoencoder accurately is caused by the problems encountered by the  $\varepsilon$ -predictin DAE trained with Sc-4 in Section 4.2 of the main paper.

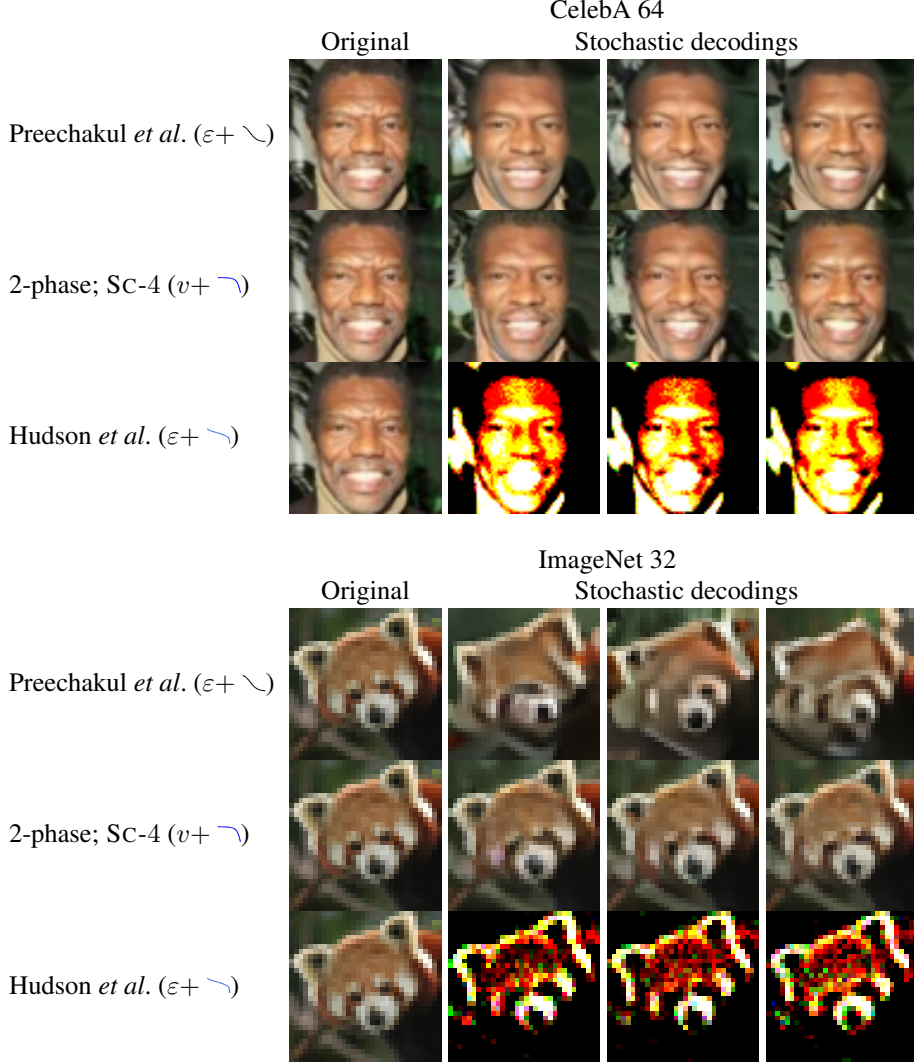


Figure 11. Some reconstructions of images from the CelebA and ImageNet datasets by models trained with the baseline training method, our proposed method, and Hudson *et al.*’s noise schedule.

## 10. Computation of Perceptual Path Length

The perceptual path length (PPL) metric was introduced by Karras *et al.* [32] to measure smoothness of image changes due to interpolation of latent codes. It is defined as

$$\text{PPL} := \frac{1}{\varepsilon^2} E_{t \sim \mathcal{U}([0, 1 - \varepsilon])} \left[ d\left(G(\text{Slerp}(\mathbf{z}_1, \mathbf{z}_2; t)), G(\text{Slerp}(\mathbf{z}_1, \mathbf{z}_2, t + \varepsilon))\right) \right]. \quad (1)$$

Here,  $\mathbf{z}_1$  and  $\mathbf{z}_2$  are the latent codes being interpolated with spherical linear interpolation, which is denoted by the  $\text{Slerp}(\cdot, \cdot; \cdot)$  function in the equation above.  $G$  denotes a generator, which is a function that is capable of turning a latent code into an image. The function  $d(\cdot, \cdot)$  is a distance function between two images, and Karras *et al.* implemented it with the LPIPS metrics [90] computed with a VGG network [64]. Lastly,  $\varepsilon$  is a small constant, which Karras *et al.* uses  $10^{-4}$ . The expectation is taken over the random variable  $t$ , the interpolation “time,” which is sampled uniformly from the interval  $[0, 1 - \varepsilon]$ .

Equation (1) is an approximation of the integral

$$\frac{1}{\varepsilon^2} \int_{t=0}^1 \left[ \lim_{\Delta t \rightarrow 0} \frac{d(G(\text{Slerp}(\mathbf{z}_1, \mathbf{z}_2; t)), G(\text{Slerp}(\mathbf{z}_1, \mathbf{z}_2, t + \Delta t)))}{\Delta t} \right] dt$$

by Monte Carlo integration. We made the calculation deterministic by dividing  $[0, 1]$  into  $N$  subintervals, each of length  $1/N$ . Then, we compute the integral for each interval and add the results up. In other words,

$$\begin{aligned} \text{PPL} &= \frac{1}{\varepsilon^2} \sum_{i=0}^{N-1} \int_{t=i/N}^{(i+1)/N} \left[ \lim_{\Delta t \rightarrow 0} \frac{d(G(\text{Slerp}(\mathbf{z}_1, \mathbf{z}_2; t)), G(\text{Slerp}(\mathbf{z}_1, \mathbf{z}_2, t + \Delta t)))}{\Delta t} \right] dt \\ &\approx \frac{1}{\varepsilon^2} \sum_{i=0}^{N-1} \frac{d(G(\text{Slerp}(\mathbf{z}_1, \mathbf{z}_2; i/N)), G(\text{Slerp}(\mathbf{z}_1, \mathbf{z}_2, (i+1)/N)))}{N}. \end{aligned}$$

Lastly, we set  $\varepsilon = 1/N$ , yielding

$$\text{PPL} := N \sum_{i=0}^{N-1} d(G(\text{Slerp}(\mathbf{z}_1, \mathbf{z}_2; i/N)), G(\text{Slerp}(\mathbf{z}_1, \mathbf{z}_2, (i+1)/N))).$$

In Section 5.2, we use  $N = 100$ .

## 11. Additional Results on Information with Latent Codes

We show AUROC values of CelebA attributes in Table 10 and CIFAR-10 classes in Table 11

Attribute	Preechakul <i>et al.</i>	1-phase; Sc-4 (↻)	2-phase; Sc-4 (↻)
5_o_Clock_Shadow	0.9416 (2)	0.9419 (1)	0.9356 (3)
Arched_Eyebrows	0.8986 (1)	0.8948 (3)	0.8957 (2)
Attractive	0.9060 (2)	0.9070 (1)	0.9019 (3)
Bags_Under_Eyes	0.8758 (2)	0.8759 (1)	0.8732 (3)
Bald	0.9881 (2)	0.9884 (1)	0.9834 (3)
Bangs	0.9824 (2)	0.9829 (1)	0.9743 (3)
Big_Lips	0.7661 (1)	0.7634 (2)	0.7619 (3)
Big_Nose	0.8747 (1)	0.8739 (2)	0.8723 (3)
Black_Hair	0.9354 (1)	0.9320 (2)	0.9196 (3)
Blond_Hair	0.9794 (1)	0.9784 (2)	0.9727 (3)
Blurry	0.9659 (3)	0.9683 (1)	0.9660 (2)
Brown_Hair	0.8572 (1)	0.8538 (2)	0.8216 (3)
Bushy_Eyebrows	0.9288 (1)	0.9272 (2)	0.9235 (3)
Chubby	0.9464 (2)	0.9465 (1)	0.9403 (3)
Double_Chin	0.9577 (1)	0.9565 (2)	0.9528 (3)
Eyeglasses	0.9965 (2)	0.9969 (1)	0.9959 (3)
Goatee	0.9745 (1)	0.9740 (2)	0.9707 (3)
Gray_Hair	0.9869 (1)	0.9860 (2)	0.9835 (3)
Heavy_Makeup	0.9762 (1)	0.9758 (2)	0.9734 (3)
High_Cheekbones	0.9434 (1)	0.9433 (2)	0.9400 (3)
Male	0.9967 (1)	0.9965 (2)	0.9963 (3)
Mouth_Slightly_Open	0.9816 (1)	0.9788 (3)	0.9797 (2)
Mustache	0.9656 (2)	0.9667 (1)	0.9644 (3)
Narrow_Eyes	0.8795 (1)	0.8778 (2)	0.8766 (3)
No_Beard	0.9728 (2)	0.9729 (1)	0.9695 (3)
Oval_Face	0.7463 (2)	0.7484 (1)	0.7411 (3)
Pale_Skin	0.9703 (2)	0.9704 (1)	0.9670 (3)
Pointy_Nose	0.7856 (1)	0.7843 (2)	0.7792 (3)
Receding_Hairline	0.9350 (1)	0.9331 (2)	0.9262 (3)
Rosy_Cheeks	0.9624 (2)	0.9624 (1)	0.9576 (3)
Sideburns	0.9797 (1)	0.9797 (2)	0.9745 (3)
Smiling	0.9810 (1)	0.9803 (3)	0.9804 (2)
Straight_Hair	0.7966 (1)	0.7921 (2)	0.7643 (3)
Wavy_Hair	0.8802 (1)	0.8782 (2)	0.8548 (3)
Wearing_Earrings	0.9014 (1)	0.8980 (2)	0.8816 (3)
Wearing_Hat	0.9935 (1)	0.9929 (2)	0.9865 (3)
Wearing_Lipstick	0.9835 (1)	0.9829 (2)	0.9816 (3)
Wearing_Necklace	0.7984 (1)	0.7971 (2)	0.7928 (3)
Wearing_Necktie	0.9441 (1)	0.9409 (2)	0.9372 (3)
Young	0.9150 (2)	0.9151 (1)	0.9107 (3)
<b>Average</b>	0.9263 (1)	0.9254 (2)	0.9195 (3)

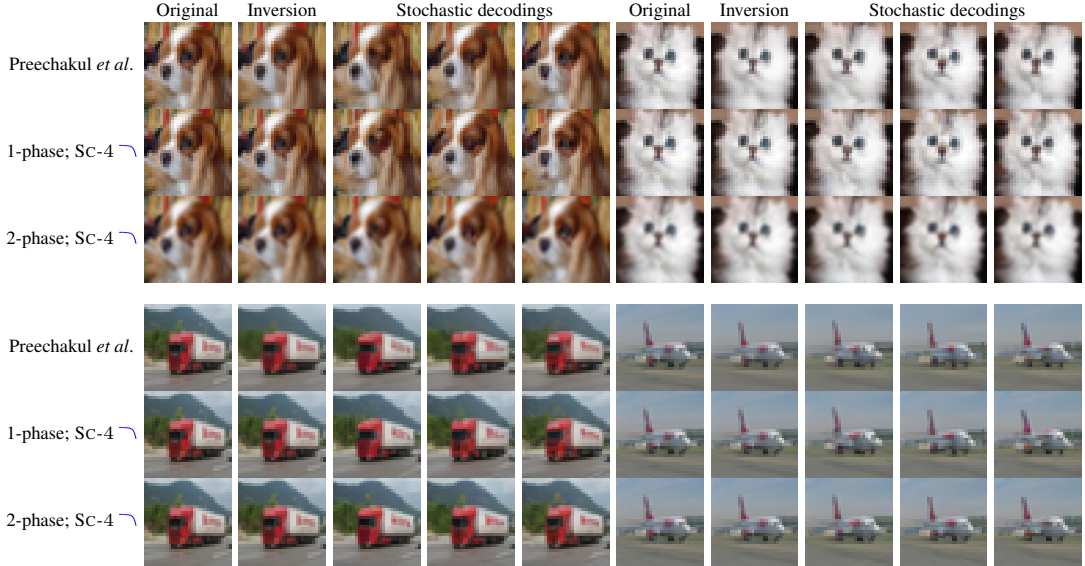
Table 10. AUROC Values for CelebA attributes. The numbers in parentheses are the ranks of individual AUROC values when they are compared to corresponding numbers of other training methods.

Class	Preechakul <i>et al.</i>	1-phase; Sc-4 (undo)	2-phase; Sc-4 (undo)
airplane	0.9720 (2)	0.9701 (3)	0.9724 (1)
automobile	0.9830 (2)	0.9813 (3)	0.9837 (1)
bird	0.9347 (1)	0.9298 (2)	0.9281 (3)
cat	0.9192 (2)	0.9119 (3)	0.9205 (1)
deer	0.9609 (1)	0.9494 (3)	0.9515 (2)
dog	0.9428 (2)	0.9360 (3)	0.9437 (1)
frog	0.9785 (2)	0.9781 (3)	0.9812 (1)
horse	0.9714 (2)	0.9664 (3)	0.9722 (1)
ship	0.9839 (1)	0.9795 (3)	0.9799 (2)
truck	0.9774 (2)	0.9766 (3)	0.9786 (1)
<b>Average</b>	0.9624 (1)	0.9579 (3)	0.9612 (2)

Table 11. AUROC Values for CIFAR-10 classes. The numbers in parentheses are the ranks of individual AUROC values when they are compared to corresponding numbers of other training methods.

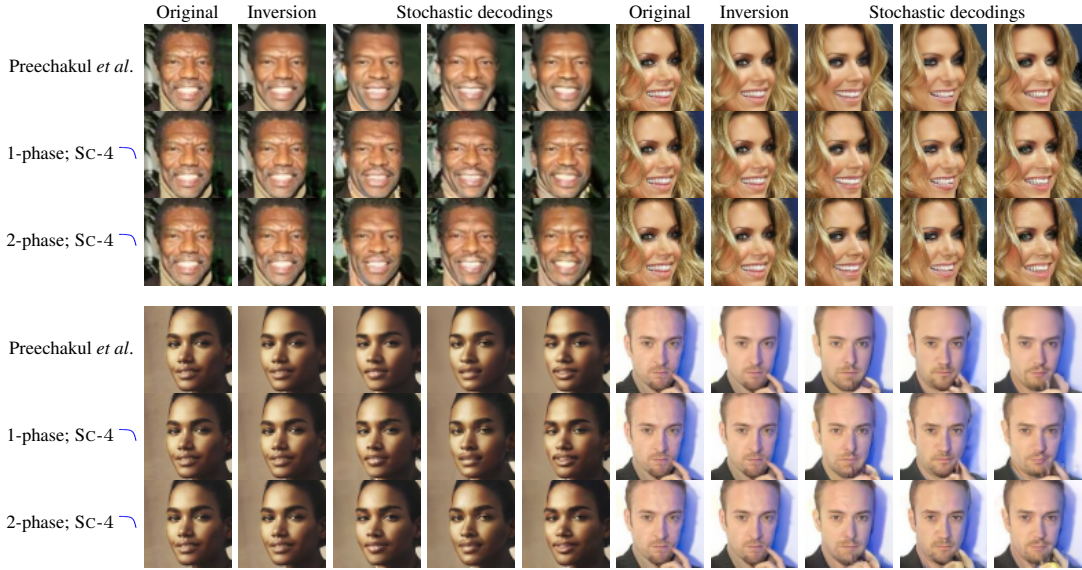
## 12. Reconstruction Results

### 12.1. CIFAR-10 32



CIFAR-10 is a small dataset (50K examples) of small images ( $32 \times 32$ ), and so the 512-dimensional latent codes seem to have captured almost all of the image information, save for extremely fine details. Hence, reconstructions by all DAEs are already very close to the originals. We can observe minor differences between them only if we look carefully enough.

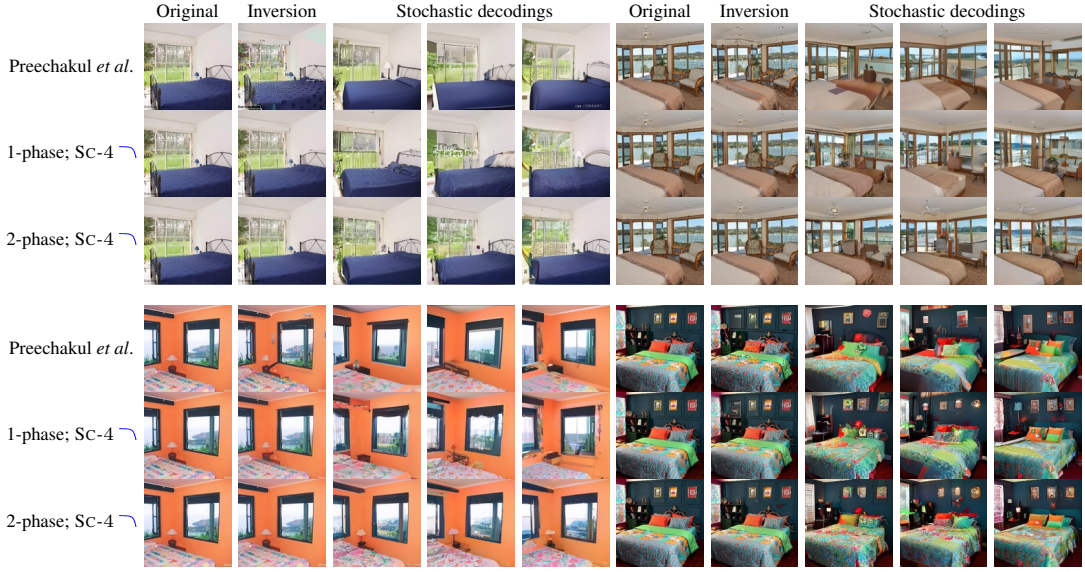
## 12.2. CelebA 64



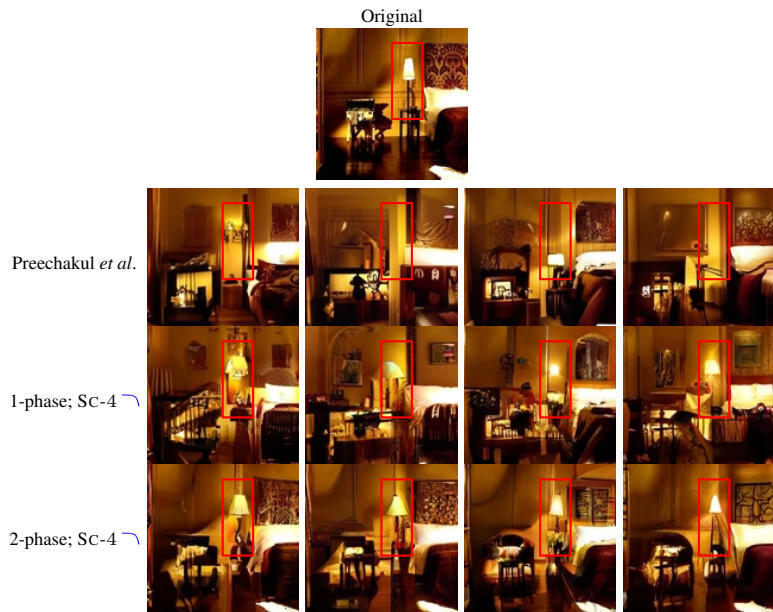
For the CelebA dataset, the 1-phase training method with Sc-4 (blue curved arrow) and our proposed 2-phase training method produced sharper images compared to those of Preechakul *et al.*'s method. We show examples of stochastic decodings that highlight differences in sharpness below.

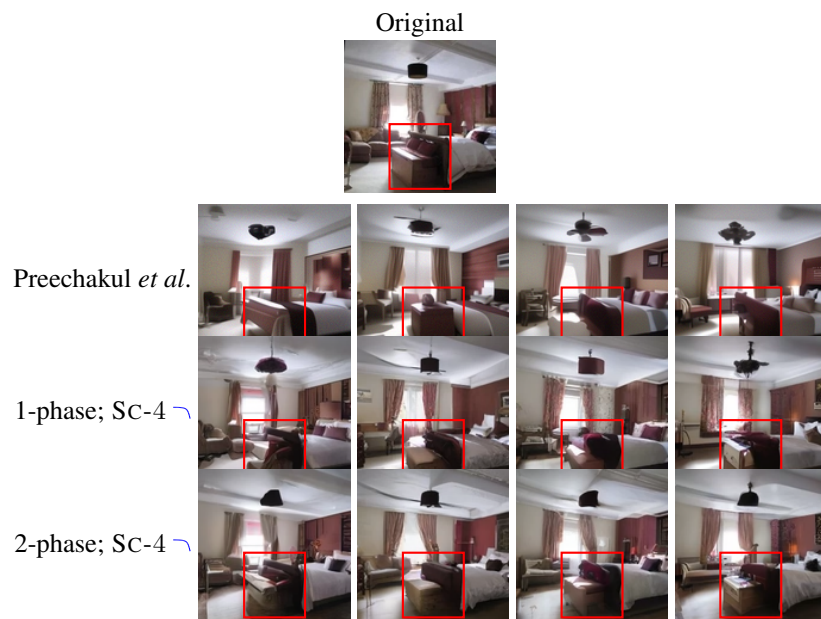
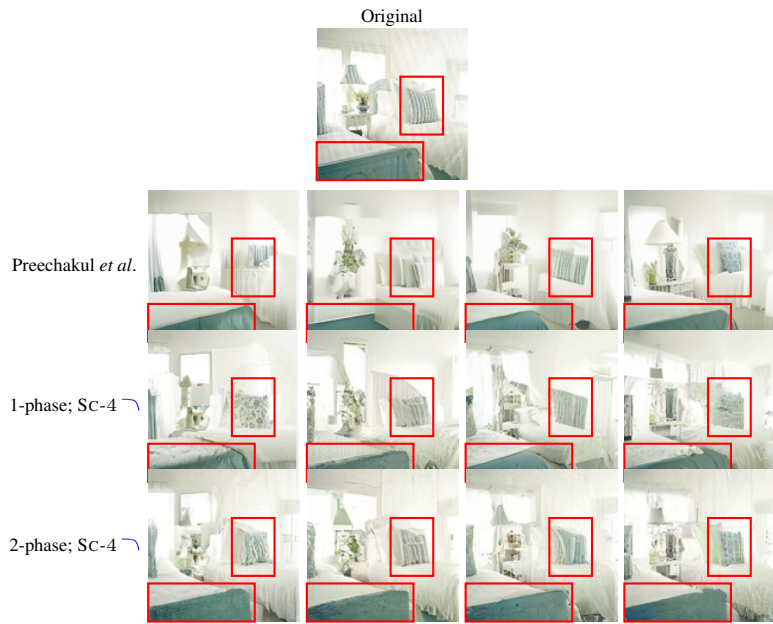


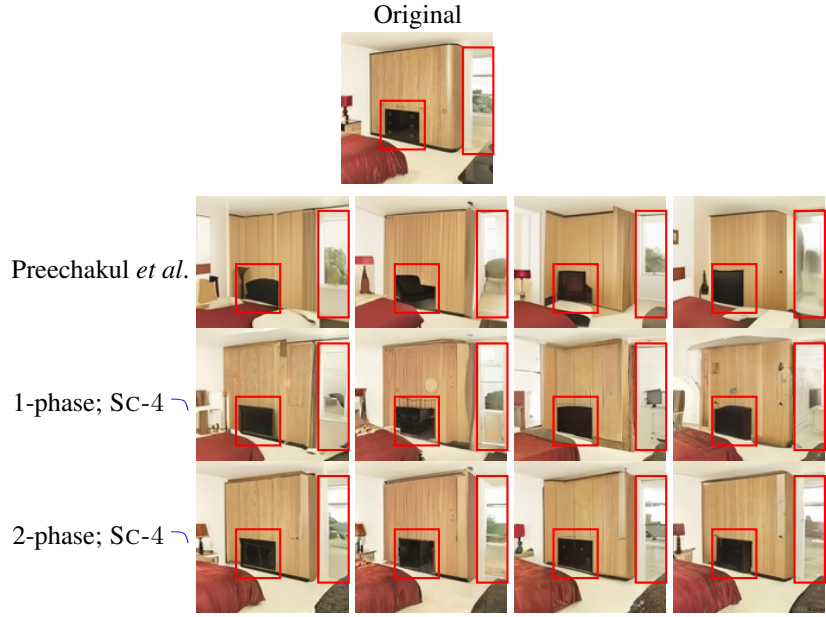
### 12.3. LSUN Bedroom 128



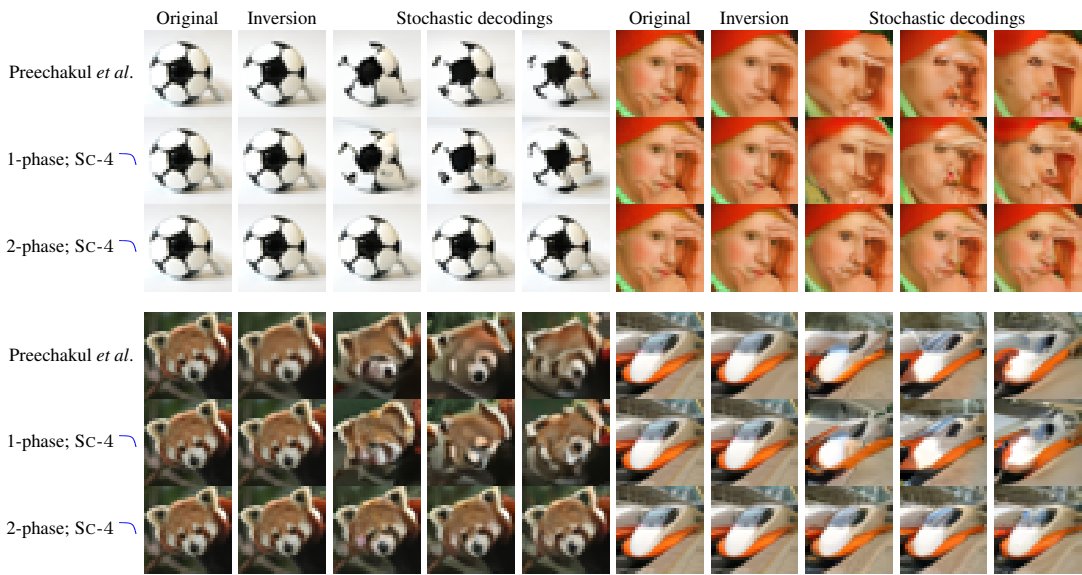
LSUN Bedroom was the largest dataset we evaluated in terms of amount (3M images) and image size ( $128 \times 128$ ). We found that the proposed 2-phase training method yielded the most accurate reconstructions. In the examples of stochastic decodings below, observe how our method preserved the shapes of the lamp, pillow, bed, and window while other methods sometimes distorted their shapes or made them disappear completely.







## 12.4. ImageNet 32



For ImageNet 32, our proposed method yielded much more accurate stochastic decodings than other methods, and the difference in accuracy is very noticeable. In the examples below, while other methods distort the lens of the camera, the pattern on the vase, and the faces of animals, our method yielded images that are readable and free from deformation.

